Cloud Removal From Multitemporal Satellite Images Using Information Cloning

Chao-Hung Lin, *Member, IEEE*, Po-Hung Tsai, Kang-Hua Lai, and Jyun-Yuan Chen

Abstract—A cloud removal approach based on information cloning is introduced. The approach removes cloud-contaminated portions of a satellite image and then reconstructs the information of missing data utilizing temporal correlation of multitemporal images. The basic idea is to clone information from cloud-free patches to their corresponding cloud-contaminated patches under the assumption that land covers change insignificantly over a short period of time. The patch-based information reconstruction is mathematically formulated as a Poisson equation and solved using a global optimization process. Thus, the proposed approach can potentially yield better results in terms of radiometric accuracy and consistency compared with related approaches. Some experimental analyses on sequences of images acquired by the Landsat-7 Enhanced Thematic Mapper Plus sensor are conducted. The experimental results show that the proposed approach can process large clouds in a heterogeneous landscape, which is difficult for cloud removal approaches. In addition, quantitative and qualitative analyses on simulated data with different cloud contamination conditions are conducted using quality index and visual inspection, respectively, to evaluate the performance of the proposed approach.

Index Terms—Cloud removal, information cloning, Poisson equation.

I. INTRODUCTION

GLOBALLY, the Enhanced Thematic Mapper Plus (ETM+) land scenes are, on average, about 35% cloud covered, as reported by Ju and Roy [1], indicating that cloud covers are generally present in optical satellite images. This phenomenon limits the usage of optical images and increases the difficulty of image analysis. Thus, considerable research efforts have been devoted to the topic of cloud removal to ease the difficulties caused by cloud covers [2]–[7]. If multitemporal images are acquired, the cloud-cover problem has a chance to be eased by reconstructing the information of cloud-contaminated pixels under the assumption that the land covers change insignificantly over a short period of time.

The aim of this study is to remove clouds and reconstruct information of missing data by taking advantage of the temporal correlation of multitemporal images. An information cloning algorithm is introduced to consistently reconstruct the information of cloud-contaminated region using several high-similarity and cloud-free patches acquired at different times. Instead of reconstructing information pixel by pixel [2], [3], which may have the problem of radiometric inconsistency, we propose a patch-based approach that mathematically formulates the reconstruction problem as a Poisson equation and then solve this equation using a global optimization process. In the optimization, the selected cloud-free patches are globally and consistently cloned in the corresponding cloud-contaminated region. This process potentially results in good cloud removal results in terms of radiometric accuracy and consistency.

In the past decade, a number of cloud removal approaches have been proposed. These approaches can be classified into three categories: *inpainting-based*, *multispectral-based*, and *multitemporal-based*. In the first category, without the aid of multispectral and multitemporal data, the cloud-contaminated regions are synthesized using image synthesis and inpainting techniques [4]–[6]. The information inside the cloud-contaminated region is synthesized by propagating the geometrical flow inside that region. The synthesis approaches can yield a visually plausible result, which is suitable for cloud-free visualization. However, the lack of restoring information of cloud-contaminated pixels makes them unsuitable for further applications. In multispectral-based approaches, multispectral data are utilized in cloud detection and removal [7]–[11]. Rakwatin *et al.* [7] proposed a reconstruction algorithm to restore missing data of Aqua Moderate Resolution Imaging Spectroradiometer (MODIS) band 6 using histogram matching and least squares fitting. Histogram matching corrects detector-to-detector striping of the functional detectors, and least squares fitting reconstructs the missing parts based on a cubic polynomial derived from the relation between Aqua MODIS bands 6 and 7. Chun *et al.* [8] regarded cloud removal as a denoising problem. Based on statistical characteristics of images, an improved homomorphism filtering is applied to filter out low-frequency components that potentially represent clouds. Similarly, Wang *et al.* [9] filtered out clouds in the infrared band using wavelet frequency analysis and then reconstructed information of cloud-contaminated regions for the other bands by a B-spline-based surface repairing approach. Zhang *et al.* [10] proposed a geostatistical approach to interpolate intensities of cloud-contaminated pixels using kriging or cokriging interpolation techniques. Although the aforementioned methods based on the ideas of denoising and intensity interpolation can restore cloud-contaminated pixels sometimes with very good results, such methods tend to have difficulty with large clouds. Recently, Roy *et al.* [11] have proposed to use information observed by MODIS to predict Landsat ETM+ images. In general, fusing information from different sensors is constrained by

spectral compatibility and spatial resolution. Although MODIS has comparable spectral bands with ETM+, this sensor has a much coarser spatial resolution.

Compared with the multispectral-based approaches, the multitemporal-based approaches [2], [3], [12]–[18] which rely on both temporal coherence and spatial coherence have a better ability to cope with large clouds. Melgani and Benabdelkader [2], [3] proposed a contextual prediction process to determine spectrotemporal relationships between the acquired images. The spectrotemporal relationships are inferred from cloud-free areas in the neighborhood of cloud-contaminated regions over the available temporal images. Li *et al.* [12], [13] adopted a thresholding-based approach to identify the best cloud-free and nonshadow pixels in a given region. A cloud-free image is then generated by stitching or mosaicking the selected cloud-free pixels. Gabarda and Cristóbal [14] introduced a cloud removal method based on image fusion that involves a 1-D pseudo-Wigner distribution transformation and a pixelwise cloud model. Both features can be interpreted as a denoising method centered on pixel-level measurement. Denoising enables selection of noise-free pixels from input images. Helmer and Ruefenacht [15] utilized regression tree to detect and predict pixel values underneath clouds and cloud shadows from other image data captured at different times. An improved histogram matching was then adopted to match adjacent scenes with only spectral data and maximum likelihood classification. Similarly, Jiao *et al.* [16], Wang *et al.* [17], and Tseng *et al.* [18] corrected the radiometric inconsistency of cloud-contaminated images and their corresponding temporal images using means and standard deviations of pixel intensities first. Wavelet-based fusion method was then used to fuse boundaries of cloud-contaminated regions. While the aforementioned methods [15]–[18] can yield good results for homogeneous regions, it should be noted that the approaches based on histogram matching and data fusion tend to have difficulty with heterogeneous landscapes. Based on the shortcomings in the related works, the aim and the main contribution of this study are to reconstruct information of cloud-contaminated regions using patch-based information cloning with global optimization, which can yield better results in terms of radiometric accuracy and consistency.

II. CLOUD REMOVAL ALGORITHM

A. Overview

The workflow of the proposed cloud removal method is schematically shown in Fig. 1. Our method consists of three main processing steps: *cloud detection*, *image quality assessment*, and *information reconstruction*. In the first step, a semiautomatic cloud detection approach is adopted to detect clouds and cloud shadows for the input images. A quality assessment based on structural similarity (SSIM) index [19] is then applied to sort the input images according to image similarity. In the last step, the proposed information cloning algorithm is performed to fill in the missing data after removing the cloud-contaminated pixels.

B. Cloud and Cloud-Shadow Detection

Given a cloud-contaminated image, called target image and denoted as I_T, and a set of its corresponding images captured
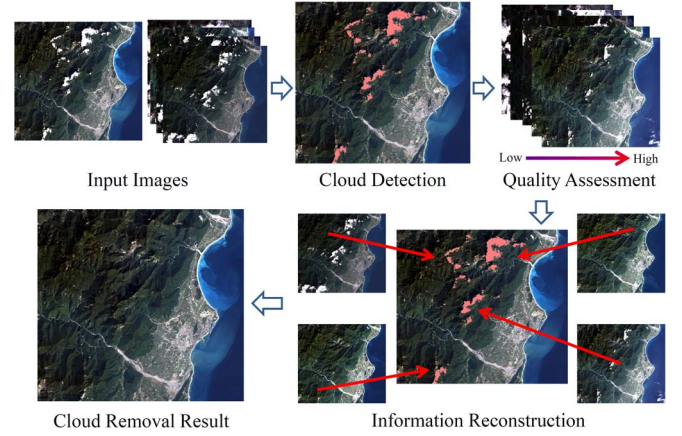

Fig. 1. Workflow of the proposed cloud removal method which consists of three main processing steps: cloud detection, image quality assessment, and information reconstruction.

at the same position but different times, called reference images and denoted as $\{I_{R_1}, \ldots, I_{R_n}\}$, the aim is to remove clouds and cloud shadows and to reconstruct the information of missing data in the target image I_T using the reference images $\{I_{R_1}, \ldots, I_{R_n}\}$. In the first step, a semiautomatic approach is adopted to detect clouds and cloud shadows in both the target and reference images. The approach presented by Huang *et al.* [20] is applied, and then, a simple user interface is provided to manually refine the detection results. In the automatic detection phase, relying on the physical fact that clouds are bright and cold in the thermal band, a thresholding-based approach is adopted to define the cloud boundaries in the spectral-temperature space. Once the cloud pixels are identified, their shadows are roughly predicted according to the cloud location and the solar illumination direction. The dark and connected components within the neighborhood of the predicted shadows are identified as the shadow components. This approach is simple and can detect most clouds and cloud shadows. To robustly generate a cloud-free and cloud-shadow-free image, a manual refinement is further performed to accurately determine the clouds and cloud shadows. In the proposed system, users are allowed to refine the cloud detection results through an interface with simple selection and erasion operations.

C. Image Quality Assessment

Once the cloud-contaminated pixels in the target and reference images are identified, several cloud-free patches are selected from the reference images $\{I_{R_1}, \ldots, I_{R_n}\}$ to reconstruct the information of cloud-contaminated regions in the target image I_T. Taking radiometric accuracy into account, the cloud-free patches are selected based on image similarity. The simplest and most widely used similarity metric is the mean square error (MSE), which is computed by averaging the squared intensity differences of pixels in the target and reference images. The MSE can be simply calculated and has a clear physical meaning. However, this metric does not fully take structure similarity into account. To generate a satisfactory cloud-free image, the SSIM index introduced by Wang *et al.* [19] is used to estimate the quality of working regions in the reference images. The SSIM index is briefly described in the following formulas, wherein this similarity measurement

has three components, namely, illumination $\mathcal{L}(I_T, I_R)$, contrast $\mathcal{C}(I_T, I_R)$, and structure $\mathcal{S}(I_T, I_R)$:

$$\mathcal{L}(I_T, I_R) = \frac{2\mu_{I_T}\mu_{I_R} + C_1}{\mu_{I_T}^2 + \mu_{I_R}^2 + C_1}$$
$$\mathcal{C}(I_T, I_R) = \frac{2\sigma_{I_T}\sigma_{I_R} + C_2}{\sigma_{I_T}^2 + \sigma_{I_R}^2 + C_2}$$
$$\mathcal{S}(I_T, I_R) = \frac{\sigma_{I_T I_R} + C_3}{\sigma_{I_T}\sigma_{I_R} + C_3} \quad (1)$$

where μ_I and σ_I represent the mean intensity and the standard deviation of image I, respectively, and $\sigma_{I_T I_R}$ represents the co-variance coefficient between images I_T and I_R. The constants C_1, C_2, and C_3 are used to avoid instability when the denom-inators are nearly zero. By combining these three similarity components, the SSIM index is formulated as follows:

$$SSIM(I_T, I_R) = [\mathcal{L}(I_T, I_R)]^\alpha [\mathcal{C}(I_T, I_R)]^\beta [\mathcal{S}(I_T, I_R)]^\gamma \quad (2)$$

where α, β, and γ are the weighting factors for the similarity components. Following the parameter setting given in [19], the weighting factors are all set to 1.0, and $C_3 = C_2/2$. This results in the following simplified form of SSIM index:

$$SSIM(I_T, I_R) = \frac{(2\mu_{I_T}\mu_{I_R} + C_1)(2\sigma_{I_T I_R} + C_2)}{\left(\mu_{I_T}^2 + \mu_{I_R}^2 + C_1\right)\left(\sigma_{I_T}^2 + \sigma_{I_R}^2 + C_2\right)}. \quad (3)$$

In the experiments, the constants C_1 and C_2 are set to $(K_1 L)^2$ and $(K_2 L)^2$, respectively, where L is the dynamic range of pixels (i.e., 255 for an 8-bit channel) and $K_1 = K_2 = 0.01$. The SSIM index ranges from 1.0 (the most similar) to -1.0 (the most dissimilar). To accurately estimate image similarity and to select suitable cloning patches, the SSIM index between the target and reference images is calculated for the cloud-free regions only. Moreover, to cope with large clouds in heterogeneous landscape, the information of a cloud-contaminated region is reconstructed using several patches in the reference images instead of using only one patch. In this manner, many reference images may be selected, and many patches may be embedded into the cloud-contaminated regions, which tends to have the problem of radiometric inconsistency. To solve this problem, the cloud amount is considered in the patch selection. For a reference image, if the amount of cloud in a patch is greater than a defined threshold (set to 80% for all experiments), then the patches will not be selected as candidates. For example, in Fig. 2, the working area (the cloud-contaminated area) is marked by a red circle. For this working area, the SSIM index of the reference image captured on June 29, 2002, is 0.9, and the cloud amount in the working area is greater than the defined threshold. Thus, this patch will not be selected as a candidate. A comparison of the patch selection with (right figure) and without (middle figure) the constraint of cloud amount is shown in Fig. 3. The number of selected reference images is reduced from six to four with the cloud amount constraint. The number of selected patches is reduced, resulting in better reconstruction quality in terms of radiometric consistency.
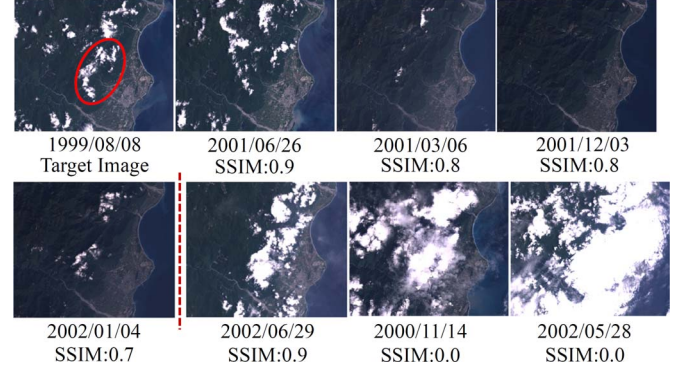

Fig. 2. Reference images sorted by SSIM index and cloud amount. The images captured on June 29, 2002, November 14, 2000, and May 28, 2002, are filtered out because of the constraint of cloud amount.
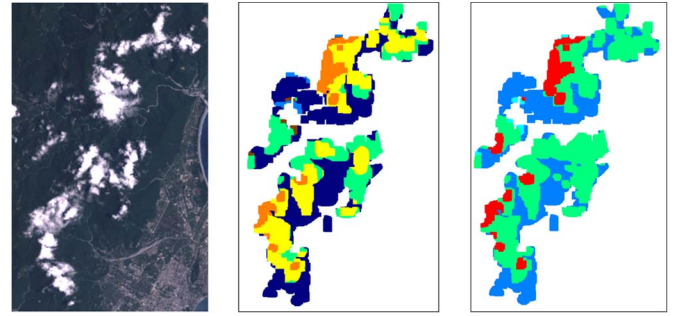

Fig. 3. Cloning patch selection. (Left) Target image. (Middle) There are six reference images selected by SSIM index. Each image is represented by a color. (Right) There are four reference images selected by SSIM index with the constraint of cloud amount.
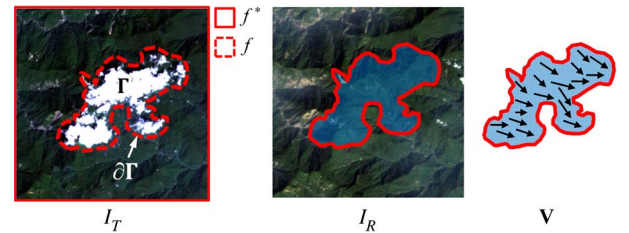

Fig. 4. Illustration of information reconstruction. The information of cloud-contaminated region Γ in target image I_T is reconstructed by the selected patch in the reference image I_R with the aid of the gradient field $\mathbf{V}$ of the selected patch.

D. Information Reconstruction

Inspired by the concept of image editing presented by Perez *et al.* [21], the details of selected patches are used to recon-struct the information of corresponding cloud-contaminated regions. Instead of correcting radiance and locally smoothing boundaries of cloud-contaminated regions or reconstructing information pixel by pixel, the problem is mathematically formulated as a Poisson equation and solved using a global optimization process. The idea is shown in Fig. 4. The cloud-contaminated region in the target image I_T is denoted as Γ, and its boundary is denoted as $\partial\Gamma$. Let f be an unknown image intensity function defined over the cloud-contaminated region Γ (i.e., the unknown that is to be calculated). Let f^* be the image intensity function defined over the target image I_T minus the cloud-contaminated region Γ, and let $\mathbf{V}$ be a guidance vector field defined over the cloud-contaminated region Γ. The vector

field $\mathbf{V}$ is defined as the gradient of the selected patches and is used to guide the reconstruction process to optimize the pixel intensities in the cloud-contaminated regions. To find an accurate and optimized reconstruction result (i.e., the solution of the unknown function f), the problem is formulated as an optimization equation with the boundary condition $f|_{\partial\Gamma} = f^*|_{\partial\Gamma}$:

$$\min_f \int\int_\Gamma |\nabla f - \mathbf{V}|^2, \qquad \text{with } f|_{\partial\Gamma} = f^*|_{\partial\Gamma} \qquad (4)$$

where $\nabla = ((\partial/\partial x), (\partial/\partial y))$ is the gradient operator and can be calculated by the following finite difference method:

$$\frac{\partial f(x,y)}{\partial x} = f(x+1, y) - f(x, y)$$
$$\frac{\partial f(x,y)}{\partial y} = f(x, y+1) - f(x, y). \qquad (5)$$

Equation (4) aims to derive result f with a gradient that is as close to the guidance vector field $\mathbf{V}$ (i.e., the details of selected patches) as possible. The solution to (4) is the unique solution of the following Poisson equation with Dirichlet boundary conditions:

$$\Delta f = div\,\mathbf{V} \text{ over } \Gamma, \qquad \text{with } f|_{\partial\Gamma} = f^*|_{\partial\Gamma} \qquad (6)$$

where $\Delta = (\partial^2/\partial x^2) + (\partial^2/\partial y^2)$ is the Laplacian operator and $div\,\mathbf{V} = (\partial v_1/\partial x) + (\partial v_2/\partial y)$ is the divergence of the vector field $\mathbf{V} = (v_1, v_2)$. Similarly, the second derivatives $\partial^2/\partial x^2$ and $\partial^2/\partial y^2$ can be calculated using the finite difference method as follows:

$$\frac{\partial^2 f(x,y)}{\partial x^2} = f(x+1, y) + f(x-1, y) - 2f(x, y)$$
$$\frac{\partial^2 f(x,y)}{\partial y^2} = f(x, y+1) + f(x, y-1) - 2f(x, y). \qquad (7)$$

Equations (4) and (6) are the fundamental formulations of information reconstruction. In these equations, the boundary condition $f|_{\partial\Gamma} = f^*|_{\partial\Gamma}$ is used to enforce boundary consistency between the scalar functions f and f^*. The equation minimization indicates that the gradient of the unknown function f^* is close, in L^2-norm, to the gradient field $\mathbf{V}$ of the selected patches. The physical meaning is to interpolate inward while enforcing the spatial variations of the unknown function f^* to the guidance field $\mathbf{V}$ as close as possible. Therefore, the minimization has a good probability of inconsistently cloning the details of selected patches to the cloud-contaminated regions, thereby resulting in a satisfactory cloud-free image with consistent and accurate radiance.

Equations (4) and (6) can be discretized by a pixel grid. Let N_p be the pixel set of the four connected neighbors of pixel p in the target image I_T, and denote $\langle p, q \rangle$ as a pixel pair such that pixel q is one of the four connected neighbors of pixel p (i.e., $q \in N_p$). Let $f(p)$ be the value of image function f at position/pixel p. The task is to compute the pixel intensities in the cloud-contaminated region Γ. The discretization of (4) yields the following discrete optimization equation:

$$\min_f \sum_{\langle p, q \rangle \cap \Gamma \neq 0} (f(p) - f(q) - v_{pq})^2,$$
$$\text{with } f(s) = f^*(s) \text{ for all } s \in \partial\Gamma \qquad (8)$$
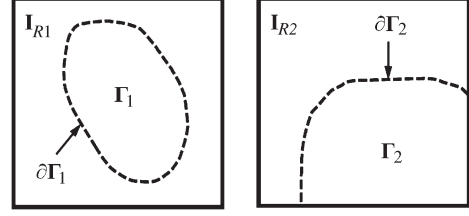

Fig. 5. Illustration of two interpolation cases. (Left) Interpolation. (Right) Extrapolation.
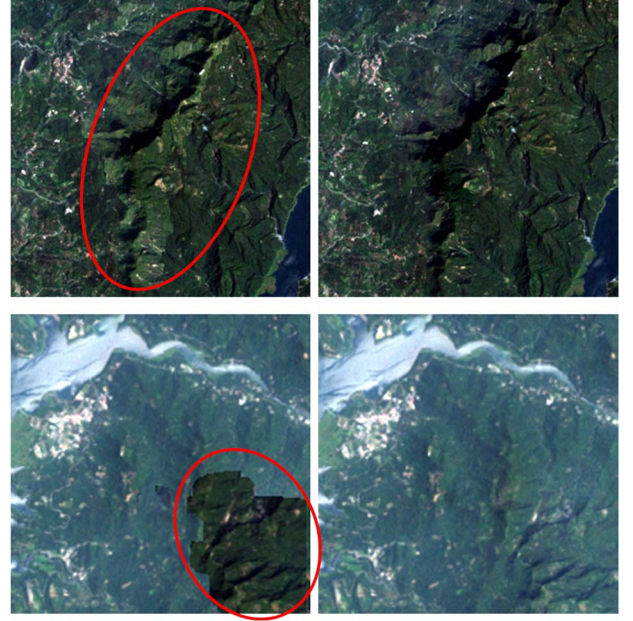

Fig. 6. Demonstration of (top figures) interpolation and (bottom figures) extrapolation. The working areas are marked by red circles. (Left) Results of replacing (the red circle) the working area by the selected patch. (Right) Our results.

where $v_{pq} = I_R(p) - I_R(q)$, which is the directional gradient (i.e., the $\overrightarrow{pq}$ direction) of the reference image at position p. According to (8), the following equation can be generalized:

$$|N_p|f(p) - \sum_{q \in N_p \cap \Gamma} f(q) = \sum_{q \in N_p \cap \partial\Gamma} f^*(q) + \sum_{q \in N} v_{pq} \text{ for all } p \in \Gamma \quad (9)$$

where $|N_p|$ is the number of neighbors in N_p. Equation (9) is iteratively solved until the unknown function f is converged. As previously mentioned, the patches are selected based on image quality/similarity. Thus, the information of cloud-contaminated region is reconstructed by several different patches in the reference images. To generate a smooth guidance field, the guidance vectors on the patch boundary are calculated by averaging the gradients of neighboring patches as follows:

$$v_{pq} = \frac{(P_{R_i}(p) - P_{R_i}(q)) + (P_{R_j}(p) - P_{R_j}(q))}{2} \qquad (10)$$

where P_{R_i} and P_{R_j} represent the neighboring patches in reference images I_{R_i} and I_{R_j}. When the cloud-contaminated region Γ contains pixels on the border of the target image (as shown in Fig. 5, right), the effect of the reconstruction process will be similar to that of extrapolation. In the implementation, due to the lack of neighbor information on the border pixels, these
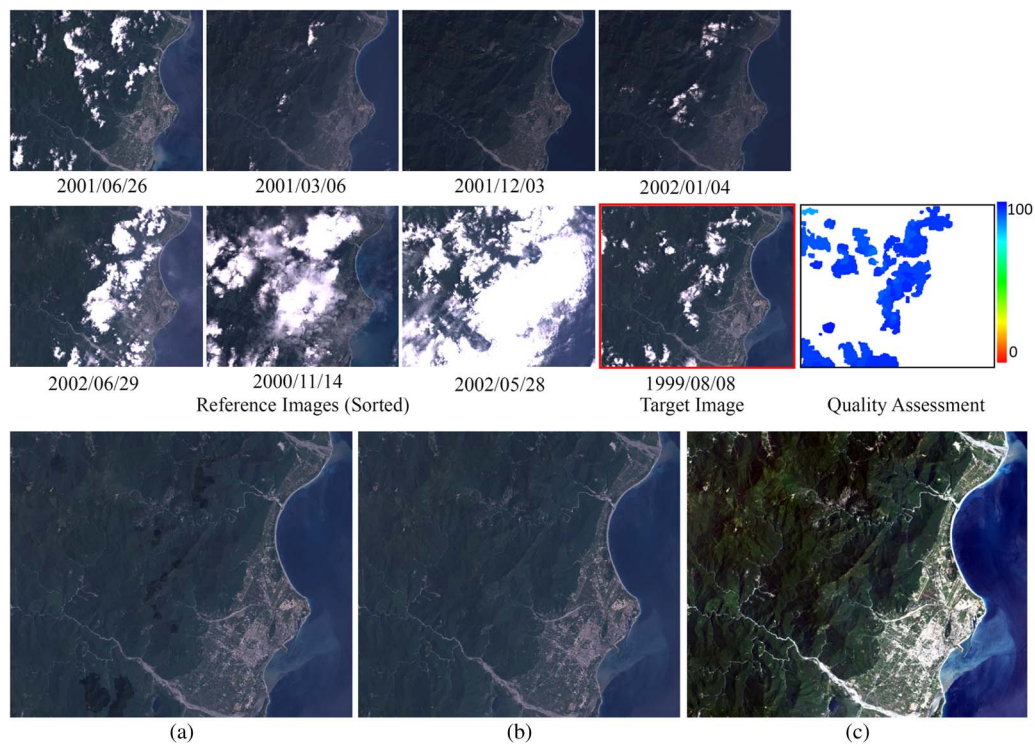
Fig. 7. Cloud removal result. (Top) (Marked by red) Target and reference images and the quality assessment of the selected patches. The reference images are sorted by SSIM index. The target image is captured near eastern Taiwan on August 8, 1999. (Bottom) (a) Result of patch replacement, (b) our result, and (c) the enhancement of (b).
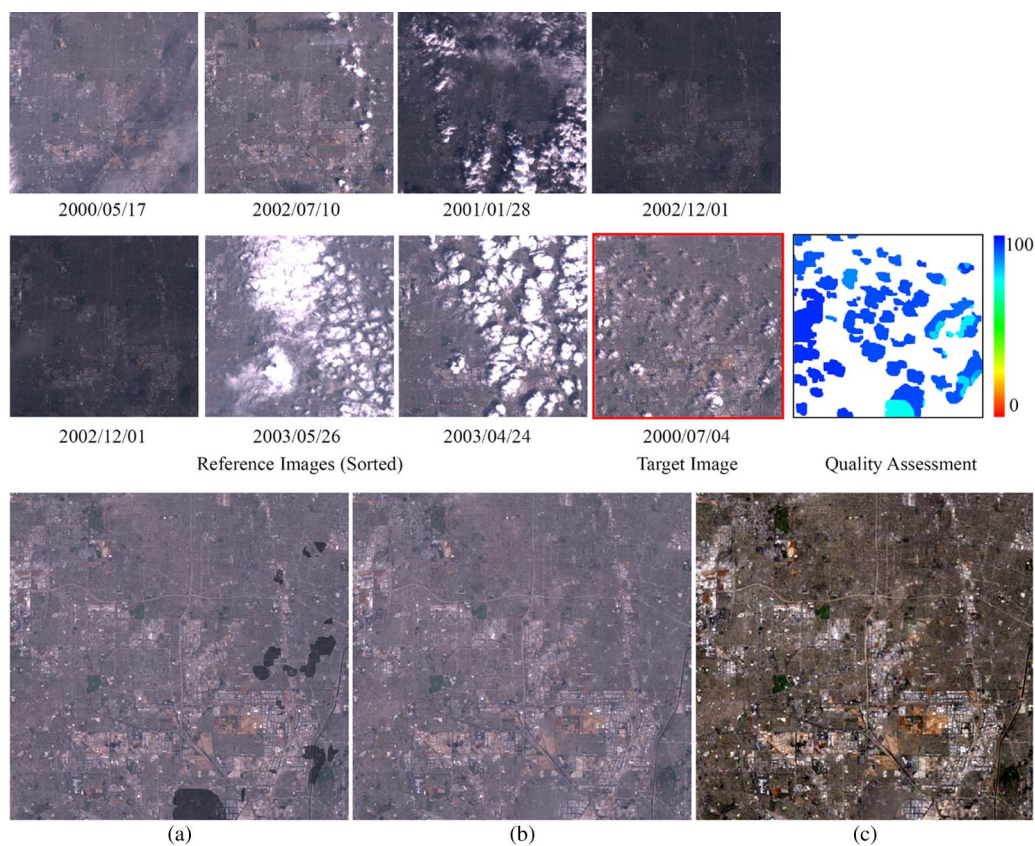
Fig. 8. Cloud removal result. (Top) Target (marked by red) and reference images and the quality assessment of the selected patches. The target image is captured near Los Angeles on July 4, 2000. (Bottom) (a) Result of patch replacement, (b) our result, and (c) the enhancement of (b).
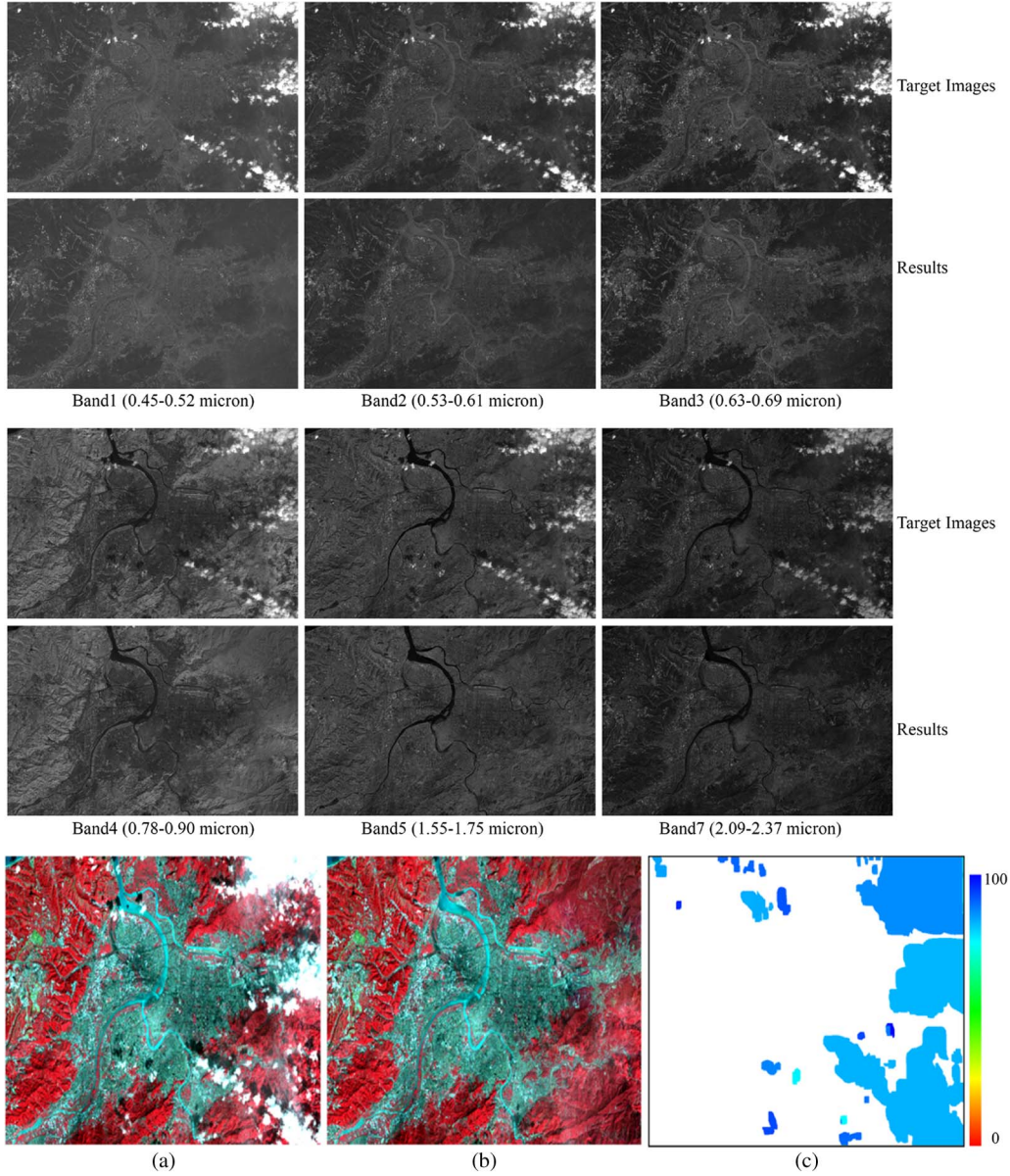
Fig. 9. Cloud removal results. (a) Target image visualized using bands 2–4. (b) Result generated by our approach. (c) Quality of the embedded patches.

pixels are calculated using (11), which removes the boundary terms in the right-hand side of (9)

$$|N_p|f_p - \sum_{q \in N} f_q = \sum_{q \in N} v_{pq}. \qquad (11)$$

The cases of interpolation and extrapolation are shown in Fig. 6. The working areas are encircled in red circles. In the top panels of Fig. 6 (the interpolation case), (9) is used to reconstruct information. In the bottom panels of Fig. 6 (the extrapolation case), the border pixels are calculated using (11), and the other pixels are calculated using (9). If the working area is replaced by a selected patch, a significant discontinuity on the brightness occurs. In contrast, the proposed approach that uses global optimization can potentially yield satisfactory results for either the interpolation case or the extrapolation case. Note that a number of works are proposed for improving or extending the gradient-based information cloning/reconstruction technique to achieve better visualization [22]–[25]. However, these approaches are unsuitable to be applied to the cloud

removal because of the lack of consideration for radiometric accuracy.

III. EXPERIMENTAL RESULTS AND DISCUSSION

Landsat-7 ETM+ images with different types of landscapes were used to test the feasibility of the proposed approach. The images captured near the east of Taiwan, Los Angeles, and Taipei in August 1999, July 2000, and November 2000 were used as inputs. The cloud removal results are shown in Figs. 7–9. In Figs. 7 and 8, the visible bands [band 1 (0.45–0.52 μm), band 2 (0.52–0.60 μm), and band 3 (0.63–0.69 μm)] of ETM+ images are used, and there are seven images selected as reference images. The cloud-free patches in the reference images with the highest rank are utilized to reconstruct the information of cloud-contaminated regions. The path quality measured by the SSIM index is normalized, and the values range from 0 (the worst quality) to 100 (the best quality). The results of patch replacement are shown in Figs. 7(a) and 8(a),
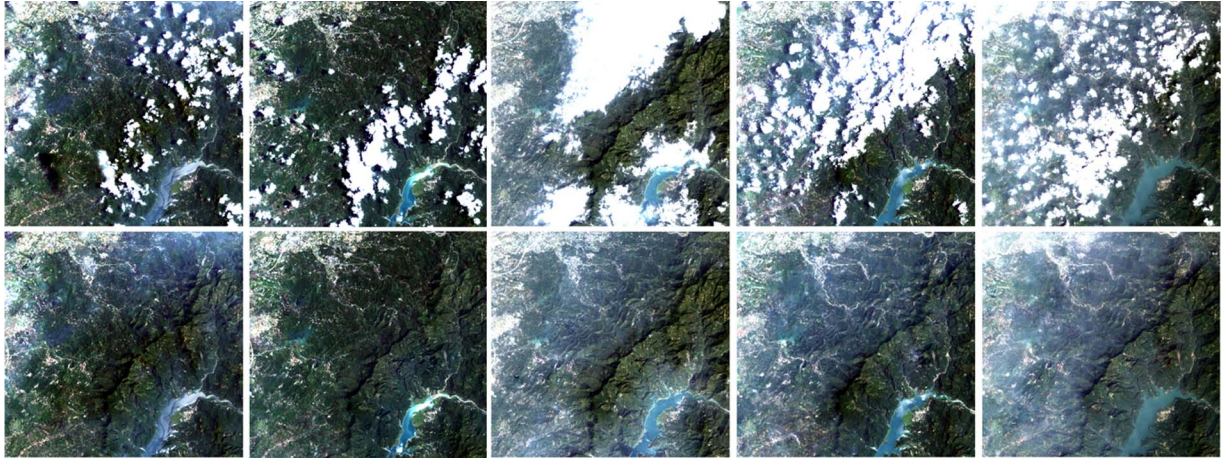
Fig. 10.   (Top) Test data. The percentages of cloud amount in the test data are 36%, 46%, 53%, 63%, and 70%, respectively. (Bottom) Cloud removal results.
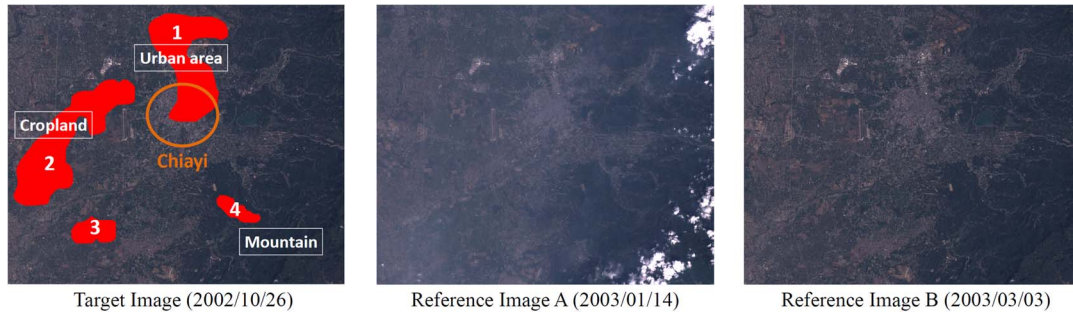

Fig. 11.   Simulation data. (Left) Target image containing four simulated cloud-contaminated regions: Area 1 (urban area and cropland), area 2 (large cropland), area 3 (small cropland), and area 4 (small mountain area). (Middle) Reference image with low dynamic range. (Right) Reference image with high dynamic range. The target image is captured near Chiayi on October 26, 2002, and the reference images are captured on January 14, 2003, and March 3, 2003.

and our results are shown in Figs. 7(b) and 8(b). The cloud-free results are enhanced by a linear enhancement transformation to provide a clear visual comparison. The enhanced results are shown in Figs. 7(c) and 8(c). In Fig. 9, bands 1–3, band 4 (0.78–0.90 μm), band 5 (1.55–1.75 μm), and band 7 (2.09–2.35 μm) of ETM+ images are used. The cloud removal result for each band and the pseudocolor image formed by bands 2–4 are shown in this figure. These results on the multitemporal images demonstrate the feasibility of our approach.

To demonstrate the robustness of our approach, we experimented on images with a large amount of cloud cover. The results are shown in Fig. 10. The images with 36%, 46%, 53%, 63%, and 70% of cloud covers were tested. With the aid of patch-based reconstruction and global optimization, satisfactory cloud-free results can be obtained even though the amount of cloud cover is large. Note that the generated results in Fig. 10 are misty because some misty patches are selected as reconstruction candidates.

An experiment of removing simulated cloud-contaminated data and reconstructing the missing data was conducted to quantify the reconstruction accuracy and to compare with the related cloud removal approaches. The experimental procedure was as follows. Select a sequence of images that contains several different landscapes, simulate clouds by partly obscuring a cloud-free image of the sequence, and then compare the reconstructed image with the original cloud-free image. A simulation image containing four simulated cloud-contaminated regions shown in Fig. 11 was tested. The experimental results and statistical analyses are shown in Fig. 12 and Table I,
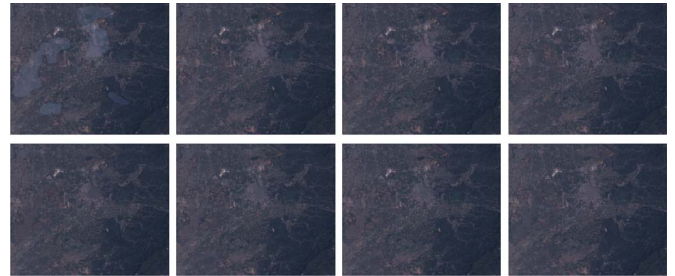

Fig. 12.   Results of cloud removal for the simulation data shown in Fig. 11. (From left to right) Results generated by patch replacement, radiometric correction, radiometric correction and boundary blending, and our approach, respectively. The results of using reference images A and B are shown at the top and bottom, respectively.

respectively. The patch replacement approach, the radiometric correction with wavelet-based color blending on boundaries suggested by Jiao et al. [16], Wang et al. [17], and Tseng et al. [18], and the proposed approach are evaluated. In [16]–[18], the process of radiometric correction is performed to correct the radiance of the cloud-contaminated image and the corresponding temporal images by the means and standard deviations of image intensities. The wavelet-based color blending/fusion is then performed to smooth the boundaries of cloud-contaminated regions. The results generated by these approaches may have a slight discontinuity at the cloud boundaries even though the smoothing operation is applied (see Fig. 12). In contrast, we formulate the reconstruction problem as a Poisson equation and solve the equation by an optimization process, yielding a better

TABLE I
RECONSTRUCTION ACCURACY OF CLOUD REMOVAL RESULTS GENERATED BY THE APPROACHES OF (APPROACH A) PATCH REPLACEMENT,
(APPROACH B) RADIOMETRIC CORRECTION, (APPROACH C) RADIOMETRIC CORRECTION AND LOCAL COLOR BLENDING,
AND OUR APPROACH. THE SIMULATION DATA AND THE REFERENCE IMAGES A AND B
(DENOTED BY RI_A AND RI_B) SHOWN IN FIG. 11 ARE USED

| Cases	Quality Index	Approach A (RI_A/RI_B)	Approach B (RI_A/RI_B)	Approach C (RI_A/RI_B)	Our approach (RI_A/RI_B)
Area 1	RMSE	7.52 / 7.04	7.01 / 6.65	6.99 / 6.61	6.28 / 6.26
	PSNR	29.85 / 29.95	30.98 / 30.99	31.01 / 31.02	32.24 / 32.25
	SSIM	0.80 / 0.80	0.83 / 0.83	0.83 / 0.83	0.85 / 0.85
Area 2	RMSE	8.11 / 7.72	7.79 / 7.13	7.77 / 7.11	7.25 / 6.96
	PSNR	29.28 / 30.15	30.30 / 31.11	30.39 / 31.14	31.01 / 31.35
	SSIM	0.55 / 0.60	0.58 / 0.63	0.58 / 0.63	0.64 / 0.65
Area 3	RMSE	7.21 / 5.82	6.85 / 5.41	6.81 / 5.36	6.54 / 5.23
	PSNR	30.50 / 32.72	31.15 / 33.27	31.20 / 33.29	31.91 / 33.80
	SSIM	0.59 / 0.73	0.62 / 0.77	0.62 / 0.77	0.64 / 0.77
Area 4	RMSE	2.88 / 3.61	2.61 / 3.12	2.60 / 3.11	2.54 / 3.05
	PSNR	38.75 / 38.01	39.89 / 38.39	39.95 / 38.41	40.11 / 38.51
	SSIM	0.88 / 0.86	0.91 / 0.88	0.91 / 0.88	0.91 / 0.88
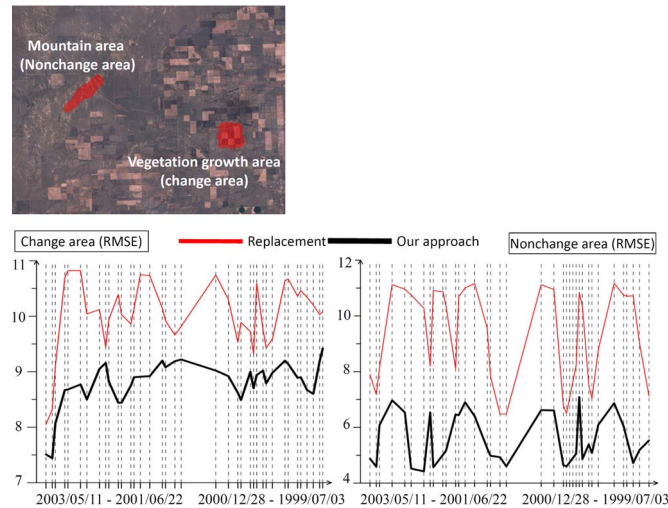
Fig. 13. Accuracy assessment for (change area) the vegetation growth area and (nonchange area) the mountain area. (Top) Target image containing two simulated cloud-contaminated areas. (Bottom) RMSE of the reconstruction results using (red curve) the patch replacement approach and (black curve) our approach with the reference images captured between July 3, 1999, and May 11, 2003.

Fig. 14. Results of cloud removal using a single reference image and multiple reference images. (a) Result of using multiple reference images (RI_A, RI_B, and RI_C). (b) Result of using a single reference image (RI_C).

result in terms of radiometric consistency. To quantitatively compare the approaches, the standard and commonly used measurements, root-mean-square error (RMSE), peak signal-to-noise ratio (PSNR), and SSIM index, are used to evaluate the results shown in Fig. 12. In this experiment, two reference images were tested for data reconstruction. Reference image B has better similarity/quality than reference image A. From the statistical table, it is apparent that the approaches using reference image B (RI_B) have better reconstruction accuracy than those using reference image A (RI_A). Moreover, our approach generally has better reconstruction accuracy compared with the related approaches. This result is particularly apparent for the case of large cloud in a heterogeneous landscape. For example, compared with the approach of radiometric correction and local color blending (i.e., approach C), our approach has a larger improvement in area 1 that contains urban areas and croplands [the RMSE is improved from 6.99 to 6.28 (11.3%)] than in area 4 that contains mountains [the RMSE is improved from 2.60 to 2.54 (2.3%)]. Note that the reconstruction quality can be greatly improved using our approach when a higher quality reference image is used or more reference images are used.
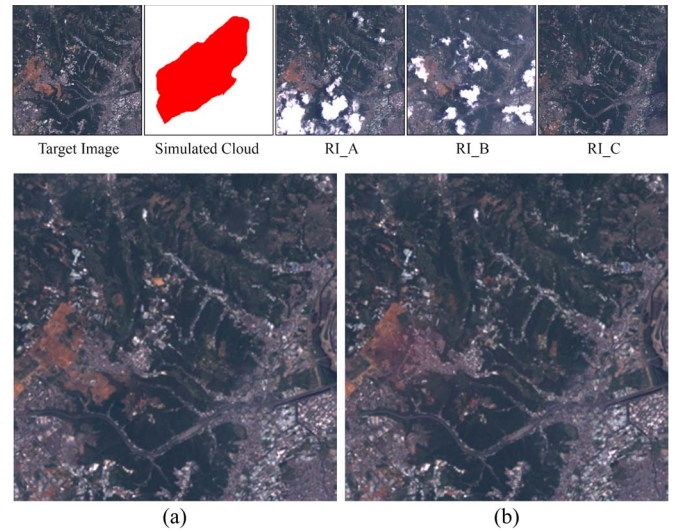
In Fig. 13, the accuracy assessment for the vegetation growth area (change area) and the mountain area (nonchange area) was conducted. The target image is captured on May 27, 2003, and the images captured between July 3, 1999, and May 11, 2003, are selected as reference images. Using our approach, the reconstruction of change area and nonchange area has average RMSE of 8.75 and 5.51, respectively. This indicates that non-harmonic changes of land cover decrease reconstruction quality. However, if the reference images captured on May 11, 2003, and April 9, 2003, are used, the reconstruction has RMSE of 7.5 and 7.43, respectively, which are close to the worst case of nonchange-area reconstruction. Therefore, our approach cannot accurately reconstruct information when land covers change significantly over a short period of time. It is a limitation of multitemporal-based approaches. For the case that land covers change nonharmonically, our approach has a chance to efficiently reconstruct information if the images captured in the period of harmonic change of land covers are selected as reference images.

To demonstrate the advantage of utilizing multitemporal images, we conducted an experiment of information reconstruction using a single reference image and multiple reference images, respectively. The results are shown in Fig. 14 and

TABLE II
RECONSTRUCTION ACCURACY OF CLOUD REMOVAL RESULTS
GENERATED USING A SINGLE REFERENCE IMAGE
AND MULTIPLE REFERENCE IMAGES

Quality Index	Single reference image (RI_C)	Multiple reference images (RI_A, RI_B, RI_C)
RMSE	6.55	6.38
PSNR	31.84	32.07
SSIM	0.80	0.89

Table II. It is apparent that using multiple reference images has better reconstruction accuracy and has comparable visual quality compared with using a single reference image.

IV. CONCLUSION AND FUTURE WORK

In this paper, a novel cloud removal algorithm has been introduced. The cloud-contaminated portions of a satellite image are removed, and then the information of missing data is reconstructed using the correlation of multitemporal images. Our approach is based on the patch-based information reconstruction strategy with the global optimization process. The major improvement is that our approach makes better use of appropriate temporal information to reconstruct the information. Thus, our approach can potentially yield better results in terms of radiometric accuracy and consistency, compared with the related approaches. Experimental analyses on sequences of images acquired by the Landsat-7 ETM+ sensor demonstrate the feasibility of our approach to process clouds in a heterogeneous landscape, and demonstrate the robustness of our approach to process images with a large amount of cloud. Moreover, the quantitative and qualitative analyses on the simulated data with different cloud contamination conditions show a clear superiority of our approach over the related approaches. In the future, an automatic cloud (including thin cloud) detection approach and a reconstruction approach for thin cloud are planned to be developed.

ACKNOWLEDGMENT

REFERENCES

[1] J. Ju and D. P. Roy, "The availability of cloud-free Landsat ETM Plus data over the conterminous United States and globally," *Remote Sens. Environ.*, vol. 112, no. 3, pp. 1196–1211, 2008.

[2] F. Melgani, "Contextual reconstruction of cloud-contaminated multitemporal multispectral images," *IEEE Trans. Geosci. Remote Sens.*, vol. 44, no. 2, pp. 442–455, Feb. 2006.

[3] S. Benabdelkader and F. Melgani, "Contextual spatiospectral postreconstruction of cloud-contaminated images," *IEEE Geosci. Remote Sens. Lett.*, vol. 5, no. 2, pp. 204–208, Apr. 2008.

[4] F. Chen, Z. Zhao, L. Peng, and D. Yan, "Clouds and cloud shadows removal from high-resolution remote sensing images," in *Proc. IEEE IGRASS*, 2005, pp. 4256–4259.

[5] A. Maalouf, P. Carre, B. Augereau, and C. Fernandez-Maloigne, "A bandelet-based inpainting technique for clouds removal from remotely sensed images," *IEEE Trans. Geosci. Remote Sens.*, vol. 47, no. 7, pp. 2363–2371, Jul. 2009.

[6] L. Lorenzi, F. Melgani, and G. Mercier, "Inpainting strategies for reconstruction of missing data in VHR images," *IEEE Geosci. Remote Sens. Lett.*, vol. 8, no. 5, pp. 914–918, Sep. 2011.

[7] P. Rakwatin, W. Takeuchi, and Y. Yasuoka, "Restoration of Aqua MODIS band 6 using histogram matching and local least squares fitting," *IEEE Trans. Geosci. Remote Sens.*, vol. 47, no. 2, pp. 613–627, Feb. 2009.

[8] F. Chun, M. Jian-wen, D. Qin, and C. Xue, "An improved method for cloud removal in ASTER data change detection," in *Proc. IEEE IGRASS*, 2004, pp. 3387–3389.

[9] Z. Wang, J. Jin, J. Liang, K. Yan, and Q. Peng, "A new cloud removal algorithm for multi-spectral images," in *Proc. SAR MIPPR*, 2005, pp. 230–240.

[10] C. Zhang, W. Li, and D. J. Travis, "Restoration of clouded pixels in multispectral remotely sensed imagery with cokriging," *Int. J. Remote Sens.*, vol. 30, no. 9, pp. 2173–2195, Jan. 2009.

[11] D. P. Roy, J. Ju, P. Lewis, C. Schaaf, F. Gao, M. Hansen, and E. Lindquist, "Multi-temporal MODIS–Landsat data fusion for relative radiometric normalization, gap filling, prediction of Landsat data," *Remote Sens. Environ.*, vol. 112, no. 6, pp. 3112–3130, Jun. 2008.

[12] M. Li, S. C. Liew, and L. K. Kwoh, "Producing cloud free and cloud-shadow free mosaic from cloudy Ikonos images," in *Proc. IEEE IGARSS*, 2003, pp. 3946–3948.

[13] M. Li, S. Liew, and L. Kwoh, "Automated production of cloudfree and cloud shadow-free image mosaics from cloudy satellite imagery," in *Proc. 20th Congr. Int. Soc. Photogramm. Remote Sens.*, 2004, pp. 15–23.

[14] S. Gabarda and G. Cristóbal, "Cloud covering denoising through image fusion," *Image Vis. Comput.*, vol. 25, no. 5, pp. 523–530, May 2007.

[15] E. Helmer and B. Ruefenacht, "Cloud-free satellite image mosaics with regression trees and histogram matching," *Photogramm. Eng. Remote Sens.*, vol. 71, no. 9, pp. 1079–1089, Sep. 2005.

[16] Q. Jiao, W. Luo, X. Liu, and B. Zhang, "Information reconstruction in the cloud removing area based on multi-temporal Chris images," in *Proc. SPIE*, 2007, p. 679 029.

[17] B. Wang, A. Ono, K. Muramatsu, and N. Fujiwara, "Automated detection and removal of clouds and their shadows from Landsat TM images," *IEICE Trans. Inf. Syst.*, vol. E82-D, no. 2, pp. 453–460, Feb. 1999.

[18] D.-C. Tseng, H.-T. Tseng, and C.-L. Chien, "Automatic cloud removal from multi-temporal spot images," *Appl. Math. Comput.*, vol. 205, no. 2, pp. 584–600, Nov. 2008.

[19] Z. Wang, A. Bovik, H. Sheikh, and E. Simoncelli, "Image quality assessment: From error visibility to structural similarity," *IEEE Trans. Image Process.*, vol. 13, no. 4, pp. 600–612, Apr. 2004.

[20] C. Huang, N. Thomas, S. N. Goward, J. G. Masek, Z. Zhu, J. R. G. Townshend, and J. E. Vogelmann, "Automated masking of cloud and cloud shadow for forest change analysis using Landsat images," *Int. J. Remote Sens.*, vol. 31, no. 20, pp. 5449–5464, Jun. 2010.

[21] P. Perez, M. Gangnet, and A. Blake, "Poisson image editing," *ACM Trans. Graph.*, vol. 22, no. 3, pp. 313–318, Jul. 2003.

[22] J. Hays and A. A. Efros, "Scene completion using millions of photographs," *ACM Trans. Graph.*, vol. 26, no. 3, pp. 87–94, Jul. 2007.

[23] M. Eitz, R. Richter, K. Hildebrand, T. Boubekeur, and M. Alexa, "Photosketcher: Interactive sketch-based image synthesis," *IEEE Comput. Graph. Appl.*, vol. 31, no. 6, pp. 56–66, Dec. 2011.

[24] A. Bugeau, M. Bertalmio, V. Caselles, and G. Sapiro, "A comprehensive framework for image inpainting," *IEEE Trans. Image Process.*, vol. 19, no. 10, pp. 2634–2645, Oct. 2010.

[25] M. Kazhdan, D. Surendran, and H. Hoppe, "Distributed gradient-domain processing of planar and spherical images," *ACM Trans. Graph.*, vol. 29, no. 2, Mar. 2010, article no. 2.

Chao-Hung Lin (M'12) received the M.S. and Ph.D. degrees in computer science and information engineering from National Cheng Kung University, Tainan, Taiwan, in 1998 and 2004, respectively.

Since 2006, he has been a Faculty Member with the Department of Geomatics, National Cheng Kung University, where he is currently an Associate Professor, leads the Digital Geometry Processing Laboratory, and coleads the Computer Graphics Laboratory. He served as an Editorial Board Member of the *International Journal of Computer Science and Artificial Intelligence*. His current research interests include remote sensing, point cloud processing, digital map generation, information visualization, and computer graphics.

Dr. Lin is a member of the Association for Computing Machinery. He served as a member of the international program committees of Pacific Graphics.
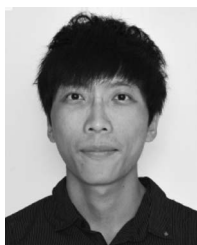
Po-Hung Tsai received the B.S. and M.S. degrees in geomatics from National Cheng Kung University, Tainan, Taiwan, in 2008 and 2010, respectively.

He is currently a member of the Digital Geometry Processing Laboratory, National Cheng Kung University. His research interests include remote sensing and image processing.

Jyun-Yuan Chen received the B.S. and M.S. degrees in geomatics from National Cheng Kung University, Tainan, Taiwan, in 2005 and 2007, respectively, where he is currently working toward the Ph.D. degree.

He is currently a member of the Digital Geometry Processing Laboratory, National Cheng Kung University. His research interests include point cloud processing, information visualization, computer graphics, remote sensing, and image processing.

Kang-Hua Lai received the B.S. degree in civil engineering from National Chung Hsing University, Taichung, Taiwan, in 2010 and the M.S. degree in geomatics from National Cheng Kung University, Tainan, Taiwan, in 2012.

He is currently a member of the Digital Geometry Processing Laboratory, National Cheng Kung University. His research interests include remote sensing and image processing.